

Article

Nanoscale Automated Quantitative Mineralogy: A 200-nm Quantitative Mineralogy Assessment of Fault Gouge Using Mineralogic

Shaun Graham ¹ and Nynke Keulen ^{2,*}

¹ Carl Zeiss Microscopy GmbH, ZEISS Group, 50 Kaki Bukit Place, Singapore 415926, Singapore; shaun.graham@zeiss.com

² Department of Petrology and Economic Geology, Geological Survey of Denmark and Greenland (GEUS), Øster Voldgade 10, DK-1350 Copenhagen K, Denmark

* Correspondence: ntk@geus.dk

Received: 14 August 2019; Accepted: 25 October 2019; Published: 29 October 2019



Abstract: Effective energy-dispersive X-ray spectroscopy analysis (EDX) with a scanning electron microscope of fine-grained materials (submicrometer scale) is hampered by the interaction volume of the primary electron beam, whose diameter usually is larger than the size of the grains to be analyzed. Therefore, mixed signals of the chemistry of individual grains are expected, and EDX is commonly not applied to such fine-grained material. However, by applying a low primary beam acceleration voltage, combined with a large aperture, and a dedicated mineral classification in the mineral library employed by the Zeiss Mineralogic software platform, mixed signals could be deconvoluted down to a size of 200 nm. In this way, EDX and automated quantitative mineralogy can be applied to investigations of submicrometer-sized grains. It is shown here that reliable quantitative mineralogy and grain size distribution assessment can be made based on an example of fault gouge with a heterogenous mineralogy collected from Ikkattup nunaa Island, southern West Greenland.

Keywords: scanning electron microscopy (SEM); automated quantitative analysis (AQM); spectrum quantification; signal deconvolution; fault gouge; 200-nm resolution; grain size distribution; Ikkattup nunaa; mineral maps; submicrometer

1. Introduction

1.1. Automated Quantitative Mineralogy (AQM)

Little work has been done in the use of scanning electron microscopy (SEM)-based automated quantitative mineralogy (AQM) in the evaluation of mineralogy and microstructures of fault gouges. Physicochemical processes taking place in these rocks are recorded in the mineralogy and the microstructures of the fault gouge itself. However, the subsequent mineralogical assemblages are incredibly fine-grained, and therefore it is challenging for microanalytical applications to provide a high-resolution quantitative mineralogy of a large area in order to understand these physicochemical processes.

“Automated mineralogy”, or more accurately described as automated quantitative mineralogy (AQM), has been available since the early 1980s with technologies such as QEMSCAN [1] and the more recent TIMA-X [2]. The key application area of this technique was to provide an automated and routine analysis capability to quantify the mineralogy and textures of ore mineralogy (modal mineralogy, liberation, association, etc.) to aid mineral processing plant development, optimization, and troubleshooting [1,3].

These automated mineralogy techniques control the electron beam to step across the sample surface, at a user-defined spatial resolution (i.e., 5- μm steps) acquiring unquantified energy-dispersive spectroscopy (EDX) spectrum. This unprocessed (no matrix corrections or spectrum quantification) spectrum is matched to a list of known referenced EDX spectra to provide a mineral name [2,4]. Without a direct measured chemical quantification from that analysis point, spectral fingerprinting on validated known mineral standards using external techniques such as electron microprobe is used [2,4,5].

The EDX spectrum, once acquired, is matched to the referenced spectrum from the mineral to classify the individual analysis. Whilst this technique is widely applied within AQM, it only provides a “crude” assessment of the mineralogy where elemental concentrations exceed 10 wt.% [5]. As such, this historic methodology falls short of providing a direct chemical analysis or correct analytical procedure to provide the necessary quality of analysis or standardized results.

Since the inception of AQM technologies, no significant methodological development of this capability occurred with little technological advancement despite the huge strides made in EDX technology and analytical capability. Multiple examples in the literature point toward the quantitative measurement capability of modern day EDX on major elements, which are able to achieve relative errors of less than 2% on a standardized analysis of polished samples [6,7].

However, the development of Mineralogic provides a step change in the analytical capabilities of AQM with the integration of these new EDX capabilities. This AQM software acquires an EDX spectrum, and performs matrix corrections and peak deconvolution for each analysis point. Minerals are subsequently classified based on stoichiometry values [8,9], providing new analytical capabilities for AQM and opening up new application areas. Concentrations of elements that cannot be analyzed correctly (e.g., H), can be assigned. The chemistry in each pixel is saved by the Mineralogic software, and the pixel’s mineralogy can therefore be reinterpreted after the analysis. Thus, each EDX analysis provides one pixel on the false-colored mineral map [9].

In dispersive spectrometry, fundamental electron beam interaction with the sample still poses challenges. All electron beam microanalysis users will be aware of the challenges of carrying out an analysis at low spatial resolutions. As a result of the energy of the primary electron beam (acceleration voltage; kV) hitting the sample, X-rays are generated from an interaction volume, which may consequently be measured by the SEM’s energy-dispersive X-ray spectrometer (EDX). The size of this interaction volume is a function of the primary energy of the beam and the mean atomic number of the sample, and it is usually presented as the diameter of the beam inside the sample material projected in the X-Z plane, which is also called the diameter of the footprint of the electron beam [10]. The interaction volume is larger than the diameter of the beam on the landing spot. In geological samples, typically containing silicates, interaction volumes can be in a region of 2–5 μm , with a 20-kV primary electron beam. Therefore, providing a chemical analysis and mineral classification based on an EDX spectrum can be challenging for fine-grained material, due to the “mixing” of compositions of a number of grains. For those grains, the interaction volume can result in the generation of X-rays from multiple minerals at a single point, providing complex mixed mineralogical compositions. Whilst these challenges remain, there is little alternative substitute for the quantification of such mineral assemblages, as gray level alone is not enough to separate and quantify the mineralogy and textures.

In this study, we provide a proof of concept in showing the capability of a new generation of SEM-based AQM to map the mineralogy and investigate the grain size of the fault gouge of varying composition at a 200-nm spatial EDX resolution.

1.2. Geological Background

The sample that was used for this study was collected in southern West Greenland from the northern coast of Ikkattup nunaa Island in the Ikkattoq anlanngua fjord (Figure 1). This locality is situated in the southern part of the Ravn Storø Supracrustal belt, which is intruded by a well-known Meso-Archaean Fiskenæsset anorthosite-leucogabbro complex. The fault rock sample represents an

amphibolite intercalated with orthogneiss. The amphibolite is part of the ca. 3.0 Ga Ravn Storø Supracrustal complex, whereas the intruding orthogneiss was dated to 2.88 Ga. Later tectonic activity in the area includes two folding and thrusting events during the Neo-Archaean, during which the Kvanefjeld block to the south collided with the Bjørnesund block (which includes the sample locality and the Fiskenæsset complex to the north of the outcrop). The thrust zones were reactivated in an extensional setting during the latest Neoarchaean or earliest Palaeoproterozoic, and the fault gouge studied here most likely was formed during this extensional event ([11]; and references therein).

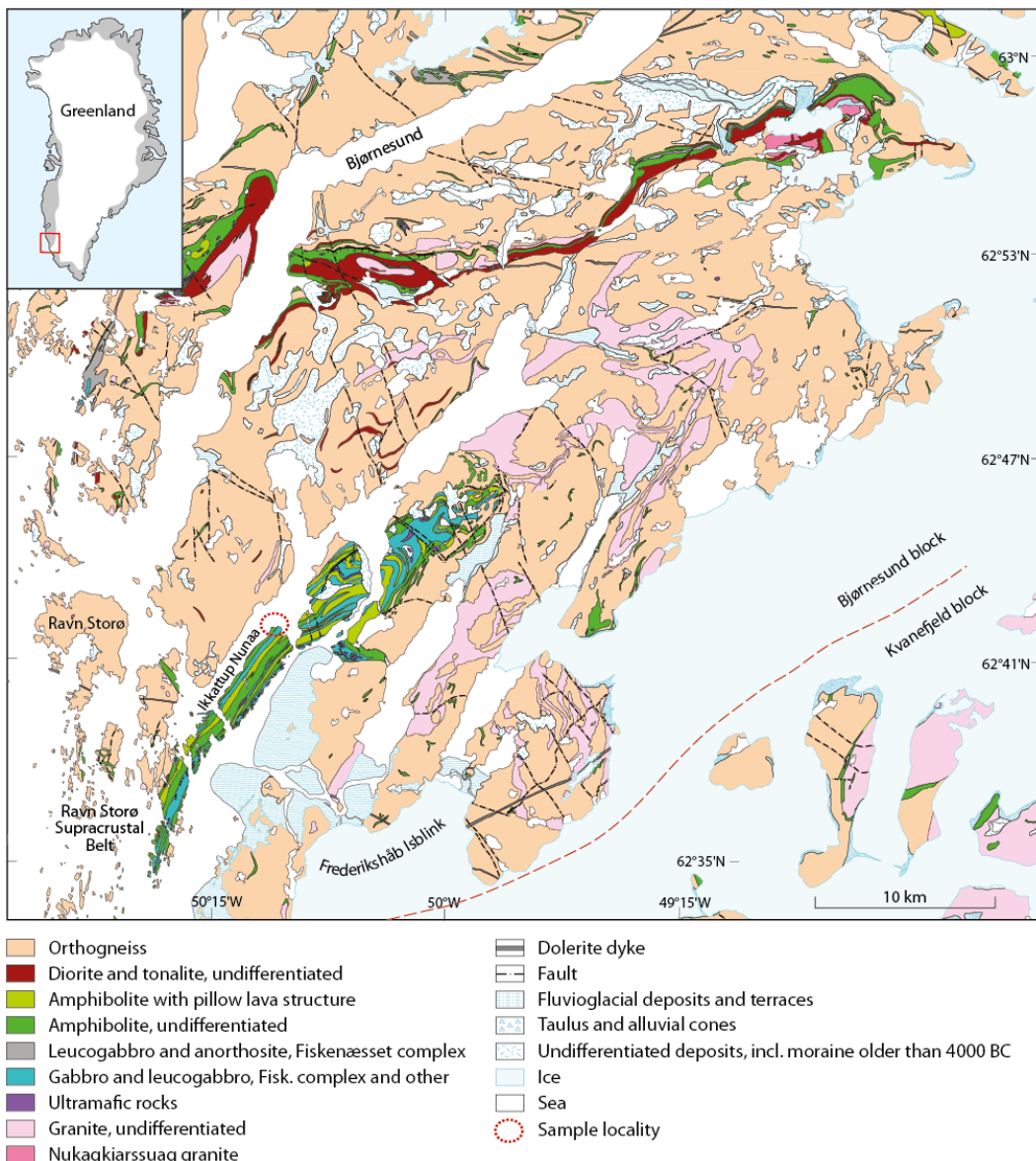


Figure 1. Geological map showing the Bjørnesund region in southern West Greenland. Sample locality, as well as the major tectonic boundary between the Bjørnesund Block and the Kvanefjeld block are indicated [12]. Map adapted from the Geological Survey of Denmark and Greenland (GEUS) [13]; reproduced with permission from GEUS.

2. Materials and Methods

The fault gouge was studied in a polished thin section and shows a mixture of grains that were originally part of the orthogneiss and of the amphibolite. Intensive mixing of the different minerals in the fault gouge prevented healing of the fault gouge to larger grain sizes [14]. Therefore, many comminuted grains of sizes smaller than 200 nm are still present in the sample. However,

mineral reactions can be observed: epidote, illite, and chlorite (chamosite) formed to replace the original mineral assembly.

To perform the microanalysis, the thin section across the fault rock was coated with carbon and studied with a Zeiss SIGMA 300VP Scanning Electron Microscope (SEM) equipped two Bruker XFlash 6/30 energy-dispersive spectroscopy detectors (EDX), with 129-eV energy resolution and with the Zeiss Mineralogic automated quantitative mineralogy software platform. The region was selected and imaged to provide a high-resolution back-scattered electrons contrast (BSE) mosaic of the region of interest. In addition, on this region of interest, a 200-nm quantitative mineralogical analysis was carried out using Mineralogic, creating a mineral map (Figure 2).

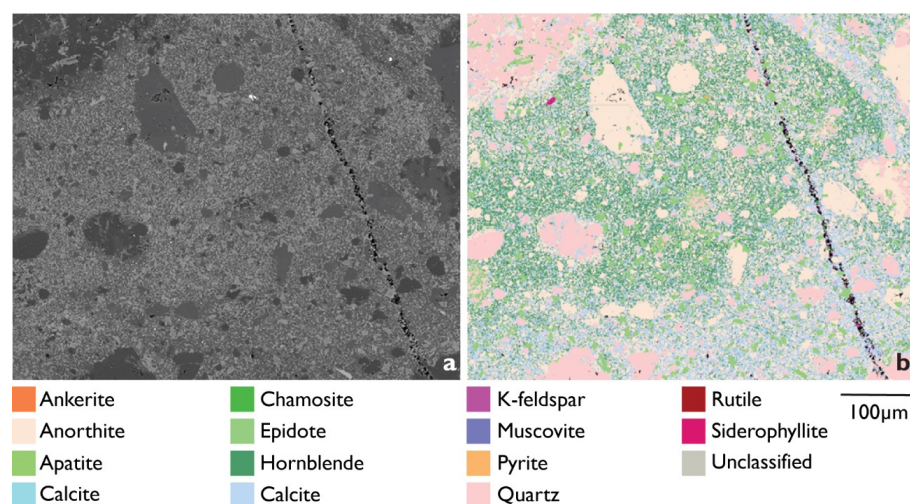


Figure 2. Large area overview image of the scanned sample area. (a) Displays the high-resolution BSE image (b) Displays the false-colored mineral map and key, displaying the mineralogy across this location.

To analyze the fine-grained fault gouge, we reduced the acceleration voltage of the primary electron beam to 10 kV to reduce the interaction volume [15–17], and therefore to minimize the amount of mixed pixel data, and used the 60- μm aperture providing a 1.8-nA beam current. Despite this reduction of primary electron energy to 10 kV, the interaction volume still has a diameter of up to approximately 1 μm for minerals with the lowest average atomic number (Z) and down to 400 nm for a high Z phase on top of a low Z phase (Figure 3). 200-nm EDX pixel size would greatly provide oversampling and a large volume of mixture pixel signatures.

Despite this, the data below outlines how the analysis and advanced mineral classifications employed in the Mineralogic mineral library were able to deconvolute any mixed signals and provide a reliable quantitative mineralogy and textural assessment. We were able to do this due to the access to fully quantitative EDX classifications for each pixel within the Mineralogic software and the ability to quantify the weight percent contribution of the elements present on a per-pixel basis (see also [9]). This enabled the creation of highly discriminatory mineral classifications whereby “contamination” of the chemical analysis provided by the above described mixed signals were able to be identified and factored into the mineral classifications of the mineral library to enable the correct classification (Figure 4). This capability and deconvolution procedure allowed the creation of true mineral classifications without the need for creating false mixed signal classifications. The mineral classifications could be used on particles down to 200 nm, even though the interaction volume of the beam was larger than 200 nm. Therefore, the obtained resolution of the analysis is 200 nm, which is the applied pixel size for the mineral, despite the larger size of the interaction volume.

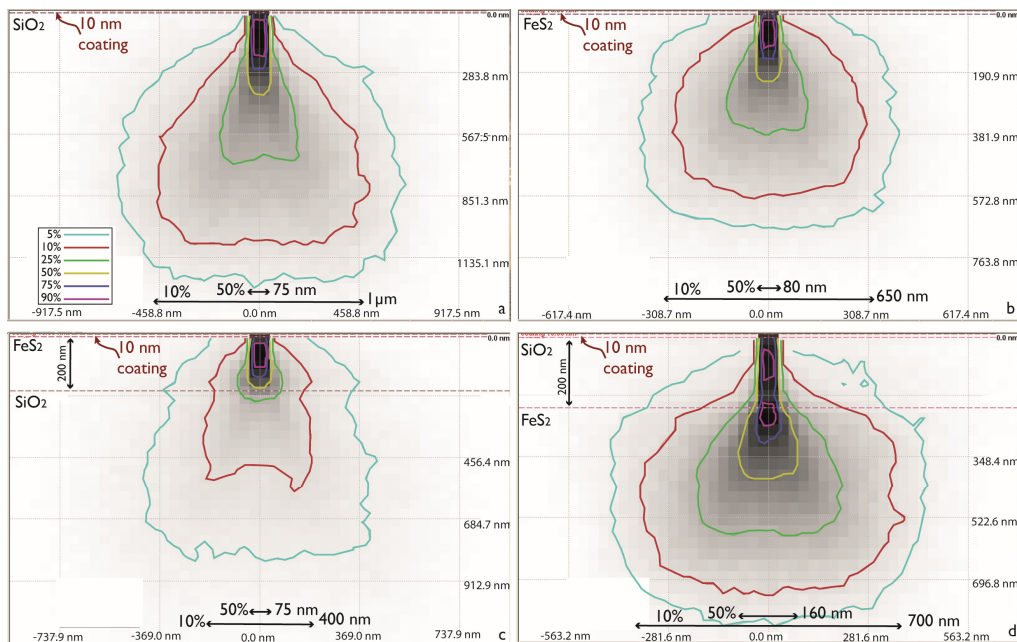


Figure 3. Monte Carlo simulations for the trajectories of 20,000 electrons in quartz (SiO_2) and pyrite (FeS_2) in carbon-coated samples. Arrows show the width of the interaction volume at 10 kV for 50% and 90% of the electrons. (a) Quartz, (b) pyrite, (c) 200-nm pyrite on top of quartz, (d) 200-nm quartz on top of pyrite. Simulations were made with Casino [18,19].

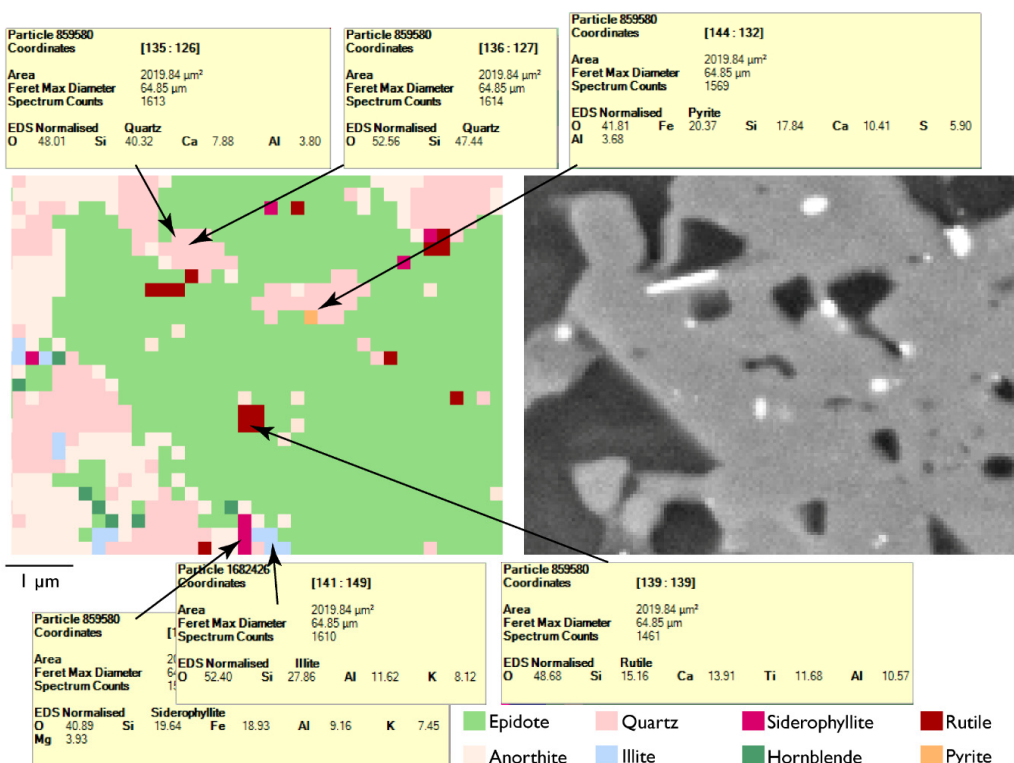


Figure 4. Detailed view of a false-colored mineral map and the associated BSE image. Each pixel represents $200 \times 200 \text{ nm}$. Grains of ca. 200 nm can be recognized and classified from the energy-dispersive spectroscopy (EDX) data for that pixel. Yellow boxes display example EDX normalized weight percentages and the interpretation of the operator for the mineralogy.

3. Results

3.1. Mineralogy

The results presented here are for a particular area of interest that is presented and displayed in Figure 2a (backscattered electron micrograph) and Figure 2b with the false-colored mineral map from Mineralogic. The analysis was carried out of a $360,000\text{-}\mu\text{m}^2$ region where a quantified EDX analysis was taken at every 200 nm, and therefore results in approximately 1.8 million quantified analyses.

Figure 2a displays the BSE data acquired from the region of interest and provides some initially information on the mineralogy based on the average atomic number of the mineral. However, the BSE gray-level intensity is not suitable to quantify mineral abundance and texture in these samples. As Figure 2a,b outlines, minerals such as illite and epidote appear to have almost identical gray-level signatures, as do hornblende, quartz, and anorthite.

However, Figure 2b displays the overlaid false-colored mineral data that was acquired at a 200-nm spatial resolution. The false-color minerals clearly display the mineralogy and the textural variation across this sample.

Combined with the modal mineralogy data (Table 1), these results clearly show how anorthite (c. 39%), illite (c. 20%), hornblende (c. 20%), and quartz (c. 13%) are the dominant mineral in this sample. It is also clear from Figure 2b and Table 1 that all the minerals show predominantly fine-grained sizes (200 nm); however, rare large clasts of quartz and anorthite are observed while hornblende, illite, and epidote mainly consist of a fine-grained matrix.

The 200-nm resolution of the scan was able to identify two distinct mineralogical and textural groups in this region (Figure 5). Textural group 1 is formed by the former amphibolite minerals and their reaction products. It can be found in the center of Figure 2, and is dominated by an epidote- and hornblende-dominated matrix that is populated with large (up to 80 microns in length) remnants of the orthogneiss, mainly consisting of single grains of quartz and anorthite. A second textural group can be found that encapsulates textural group 1 and is dominated by an illite and fine-grained anorthite matrix, which represents the remnants of the orthogneiss. In this textural group, hornblende is a minor phase in the matrix. Figure 5c,d shows that this mineralogical and textural group is dominated by anorthite, illite, and quartz with a small amount of epidote intergrown within this matrix.

3.2. Grain Size Distributions

Whilst the hornblende is relatively granular within this matrix, the epidote is often found as relatively coarse grains up to 20 microns in length (Figure 6). The anorthite grains display bimodal distribution as they are found in the matrix as grains of 1–5 microns in size, and also as much coarser remnant clasts that can be 50 microns in length or more.

The average grain size in textural group 2 is clearly much larger than that in textural group 1, and the matrix is dominated by illite and anorthite with only minor amounts of epidote and hornblende. Quartz grains are more common and of a larger grain size than those within textural group 1 (Table 2).

Table 1. Modal mineralogy data from the selected region of interest displayed in the graphical abstract. This data displays the mineral, its area % occurrence in the sample, the average grain size of that mineral with its standard deviation, and its average composition in wt.%.

Mineral	Area%	Avg Grain Size (μm)	Grain Size Std Dev (μm)	Average Composition
Anorthite	38.78	1.57	3.73	O 40.8; Si 35.62; Al 15.26; Ca 7.29; Fe 0.94; Mg 0.08; K 0.02
Illite	19.91	0.95	1.72	O 37.19; Si 31.84; Al 11.91; Fe 8.64; Ca 4.56; K 3.48; Mg 2.38
Hornblende	19.86	0.85	1.84	O 37.4; Si 31.01; Al 12.71; Fe 9.41; Ca 7.81; Mg 1.46; Ti 0.18; K 0.02
Quartz	13.27	1.11	2.62	Si 54.77; O 43.28; Al 1.95
Epidote	6.12	0.76	1.89	O 36.56; Si 25.6; Ca 16.18; Al 14.49; Fe 7.01; Mg 0.09; Ti 0.07
Siderophyllite	0.25	0.44	0.46	O 34.83; Si 22.99; Fe 19.45; Al 12.26; K 6.23; Mg 4.24
Muscovite	0.09	0.31	0.25	O 50.65; Si 30.4; Al 10.65; K 6.19; Mg 1.52; Na 0.25; Fe 0.18; Ca 0.16
Pyrite	0.08	0.44	0.32	Fe 65.19; S 34.8; Zn 0.01
Apatite	0.07	1.91	3.80	Ca 42.22; O 40.11; P 17.6; Cl 0.07; F 0
Ankerite	0.06	0.32	0.27	O 57.36; Ca 27.14; Fe 12.99; Mg 2.52
Rutile	0.05	0.52	0.34	O 65.7; Ti 34.3
Chamosite	0.02	0.61	1.02	O 33.59; Fe 24.66; Si 22.26; Al 14.33; Mg 5.03; Ca 0.13; K 0.01; Mn 0
K Feldspar	0.02	0.46	0.55	O 37.48; Si 34.62; Al 13.03; K 12.34; Ca 1.74; Fe 0.59; Mg 0.21
Calcite	0.01	0.85	0.86	O 52.63; Ca 44.23; Al 2.42; Fe 0.49; K 0.1; Mg 0.08; S 0.02; Mn 0.02

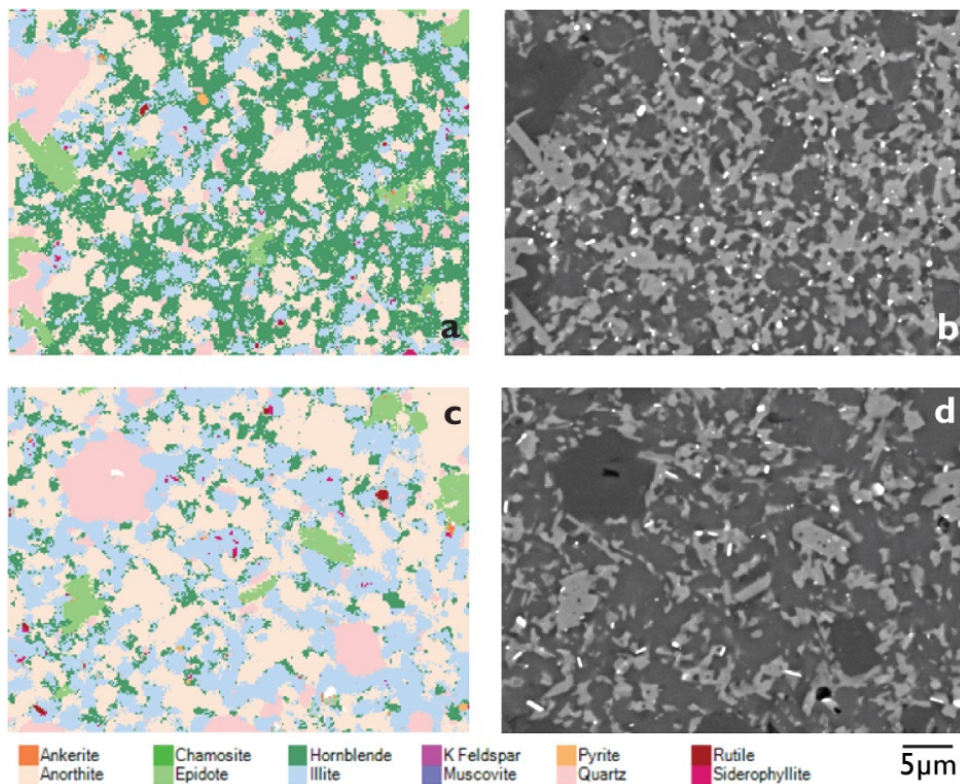


Figure 5. Two details of Figure 2: Combined false-colored mineral map (a,c) and BSE images (b,d) for textural group 1 (a,b) and textural group 2 (c,d). The width of view for each field is 46 microns.

Table 2. Modal mineralogy and grain size distribution data for textural groups 1 (TG1) and 2 (TG2) and comparative modal mineralogy and grain size distribution data for TG1 and TG2.

Mineral	Area				Average Grain Size				Grain Size Standard Distribution			
	TG1	TG2	Absolute Difference	Relative Difference (%)	TG1	TG2	Absolute Difference	Relative Difference (%)	TG1	TG2	Absolute Difference	Relative Difference (%)
Anorthite	40.68	39.92	0.76	1.89	1.55	1.62	-0.07	-4.50	3.59	4.21	-0.62	-15.94
Illite	15.14	23.46	-8.32	-43.09	0.87	1.08	-0.22	-22.26	1.26	2.23	-0.98	-55.94
Quartz	9.59	18.86	-9.27	-65.17	1.07	1.21	-0.15	-12.73	2.26	3.27	-1.01	-36.69
Hornblende	26.36	10.31	16.05	87.54	1.02	0.71	0.31	36.15	2.36	1.09	1.28	74.06
Epidote	6.23	5.49	0.74	12.62	0.61	1.40	-0.79	-78.44	1.59	2.71	-1.12	-52.18
Siderophyllite	0.20	0.29	-0.08	-34.21	0.41	0.47	-0.06	-14.16	0.46	0.50	-0.04	-7.59
Muscovite	0.07	0.12	-0.05	-54.68	0.32	0.31	0.02	4.92	0.27	0.25	0.02	7.87
Apatite	0.04	0.09	-0.06	-88.82	1.99	1.83	0.16	8.47	2.81	4.16	-1.35	-38.59
Ankerite	0.06	0.06	0.00	-0.89	0.32	0.33	0.00	-1.10	0.27	0.28	-0.01	-4.21
Pyrite	0.09	0.06	0.03	41.86	0.41	0.48	-0.08	-16.87	0.34	0.26	0.08	25.95
Rutile	0.05	0.05	0.00	-9.21	0.50	0.55	-0.05	-9.64	0.34	0.34	0.00	-0.12
Chamosite	0.01	0.04	-0.03	-127.75	0.41	0.76	-0.35	-60.31	0.68	1.17	-0.49	-52.38
K Feldspar	0.02	0.01	0.00	0.51	0.54	0.40	0.14	29.69	0.77	0.37	0.41	71.40
Calcite	0.01	0.01	0.00	-20.93	0.75	0.81	-0.07	-8.41	0.71	0.78	-0.07	-9.25

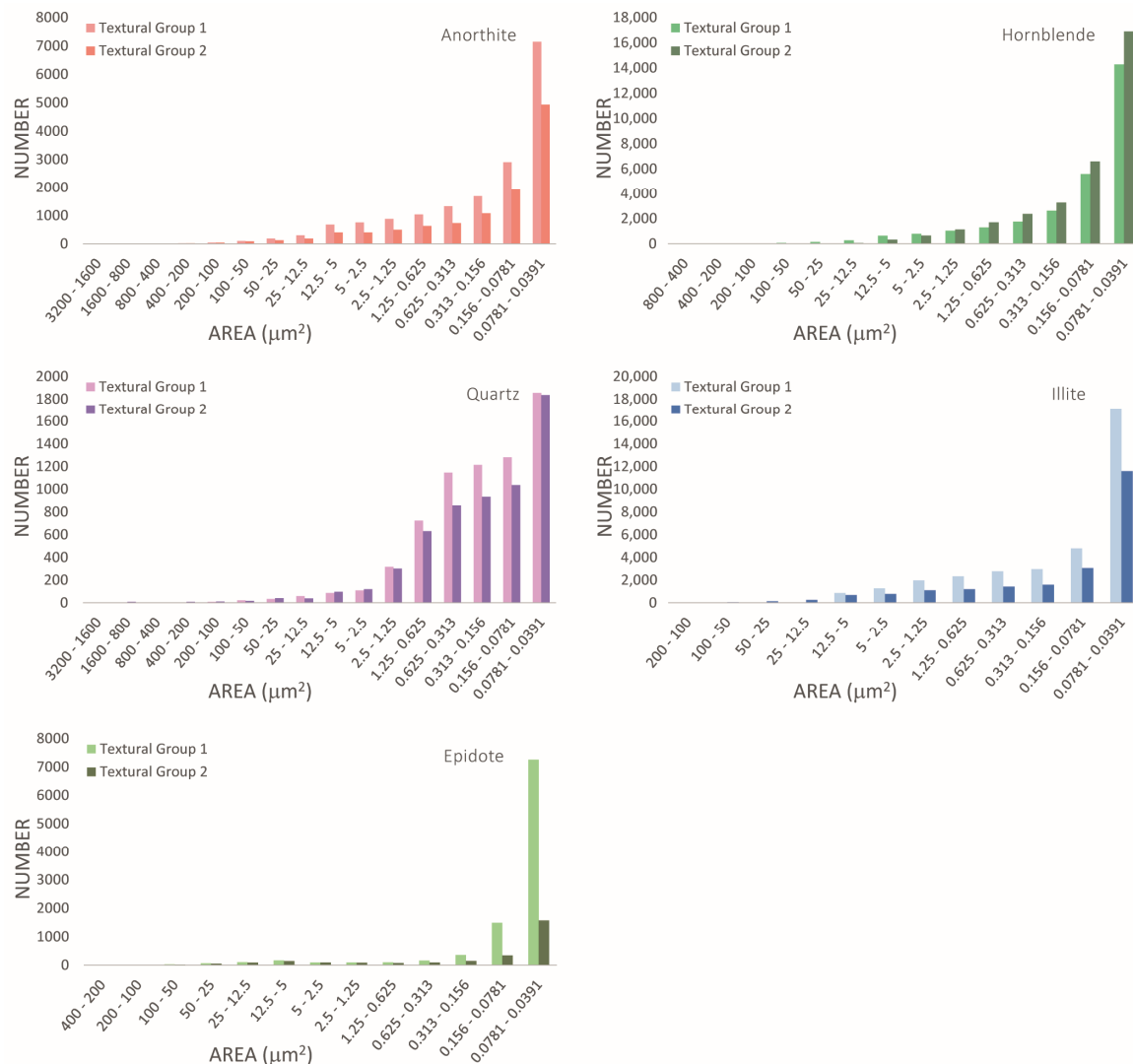


Figure 6. Grain size distribution for anorthite, hornblende, quartz, illite, and epidote in the analyzed fault gouge for textural groups 1 (TG1) and 2 (TG2). The distribution is shown as grain area in μm^2 and was measured as a 2D grain size distribution. Most grains are in the smallest bin that corresponds to grain diameters down to 200 nm.

The grain size distribution per mineral can be extracted from the Mineralogic output. Figure 6 presents the grain size distribution for one of the originally present grains, quartz, and for one of the reaction products, illite, which formed after the breakdown of feldspar minerals. Both minerals show a considerable decrease in grain size, with most grains in the bin down to 200 nm.

4. Implications

Fine-grained samples can be mapped for their mineralogy with EDX on an SEM with a step size that is considerably smaller than the diameter of the interaction volume of the primary electron beam. Whilst the BSE photomicrograph provides a higher resolution display of the region of interest, it is clearly visible that there is not enough average atomic number contrast available between the mineral phases present to clearly differentiate and quantify the mineralogy only based on the BSE image. Therefore, mineral mapping at a very high resolution is necessary to obtain most of the information on the composition of the fault gouge sample. To be able to do this, a basic understanding of the mineralogy needs to be gathered from the sample (e.g., rock type, metamorphic facies, major minerals). Building a mineral library based on the measured compositions is the initial starting point

to base classifications on for a finer pixel spacing (i.e., 200 nm) and the quantification at the nanoscale mineralogy. Whilst analyses at this resolution provided mixed pixels/signals, the ability to quantify the wt.% contribution of the elements allows for the identification and deconvolution of the mixtures and the successful classification of the mineralogy at this scale. Even for minerals with a low Z and thus a high interaction volume, which is several times larger than the size of the smallest particles and larger than the step size, a large part of the chemical information comes from the area where the beam hits the sample. Figure 3 shows that for all the investigated cases, 50% of the electron trajectories remain within a 75–160-nm wide interaction volume area and reach depths of maximum ca. 200–300 nm. Therefore, the mixed signals could successfully be identified and translated into classifications in the mineral library that enable the correct classification of those particles (Figure 4). The latter figure shows that even for 200-nm pixels, and most of the pixels at the grain boundary between two phases, the correct mineral could be determined from the mixed signal. Only one pixel away from the grain boundaries, the signal for each mineral is very near its expected composition. Compare e.g., the two yellow boxes for quartz in Figure 4.

The small step size applied for this analysis allows for an investigation of the fault gouge mineralogy at the nanometer scale with a quantification of the mineralogy to complement the BSE imaging. As EDX analyses are based on chemistry only, and the identification of the smallest grains is dependent on a beam interaction volume of a size larger than the smallest grains in the sample, X-ray diffraction or electron backscatter diffraction analyses might need to be performed in order to establish the crystallography of the minerals with an independent characterization method. This is especially important for clay minerals, which may show interstratifications at a nanometer scale, which might remain unnoticed with EDX analyses only.

The minerals in the amphibolite (anorthite, hornblende) were more intensively comminuted than the minerals in the orthogneiss (quartz, anorthite, and feldspar). Large grains of anorthite and especially quartz are still present in the sample, even though the majority of the grains were reduced to very small grain sizes. Illite is more fine-grained than quartz, which suggests that feldspar was more intensively comminuted than quartz, and that the illite grains did not grow after their formation. This brittle behavior of quartz and feldspar suggests greenschist facies temperature conditions during comminution [20,21]. Therefore, the fault gouge formed after the uplift of the area to upper-crustal levels (greenschist facies conditions) during a late stage of the geological history of the area. This is also confirmed by the observed mineral reactions of hornblende and anorthite to epidote, biotite to chamosite, and feldspar to illite, which all are typically occurring at lower greenschist facies conditions [22–24]. No large veins and no stacks of mica grains (chamosite, muscovite) or illite were observed, suggesting that these minerals grew after deformation, as a result of diagenetic processes (compare to [24]).

5. Conclusions

This study is believed to be the first recorded example of a successful automated quantitative mineralogy analysis of fault gouge to be accurately performed at such a fine pixel detail (200 nm). The ability to quantify the EDS spectrum at each analyzed point into its primary chemical components, and the use of in-built matrix corrections and peak deconvolutions, provide a robust analytical framework to provide high-quality quantitative chemical data that have never before been possible in AQM. Then, this can be used to define mineral species and use the quantified chemical capability to identify and deconvolute the mixed signals at such fine scales, despite the mixed signatures provided from the primary electron beam interaction. Therefore, the ability to map and successfully classify at such high resolutions opens up a wide range of new applications in automated quantitative mineralogy that have never before been possible.

Author Contributions: Conceptualization, S.G.; methodology, S.G.; validation, S.G. and N.K.; formal analysis, S.G.; investigation, S.G. and N.K.; resources, N.K.; writing—original draft preparation, S.G. and N.K.; writing—review and editing, S.G. and N.K.; visualization, S.G. and N.K.; project administration, S.G. and N.K.

Funding: This research received no external funding.

Acknowledgments: The authors would like to thank the three anonymous reviewers for their comments to an earlier version of this paper. The editors are thanked for their careful handling of the manuscript.

Conflicts of Interest: The authors declare no conflict of interest.

References

1. Sutherland, D.N.; Gottlieb, P. Application of automated quantitative mineralogy in mineral processing. *Min. Eng.* **1991**, *4*, 753–762. [[CrossRef](#)]
2. Hrtska, T.; Gottlieb, P.; Skála, R.; Breiter, K.; Motl, D. Automated mineralogy and petrology—Applications of Tescan Integrated Mineral Analyzer (TIMA). *J. Geosci.* **2018**, *63*, 47–63.
3. Lotter, N.-O.; Kowal, D.L.; Tuzun, M.A.; Whittaker, P.J.; Kormos, L. Sampling and flotation testing of Sudbury Basin drill core for process mineralogy modelling. *Miner. Eng.* **2003**, *16*, 857–864. [[CrossRef](#)]
4. Gottlieb, P.; Wilkie, G.; Sutherland, D.; Ho-Tun, E.; Suthers, S.; Perera, K.; Jenkins, B.; Spencer, S.; Butcher, A.; Rayner, J. Using quantitative electron microscopy for process mineralogy applications. *JOM* **2000**, *52*, 24–25. [[CrossRef](#)]
5. Andersen, J.C.Ø.; Rollinson, G.K.; Snook, B.; Herrington, R.; Fairhurst, R.J. Use of QEMSCAN® for the characterization of Ni-rich and Ni-poor goethite in laterite ores. *Min. Eng.* **2009**, *22*, 1119–1129. [[CrossRef](#)]
6. Newbury, D.E. Energy-dispersive spectrometry. In *Methods in Materials Research*; Kaufmann, E.N., Abbaschian, R., Barnes, P.A., Bocarsly, A.B., Chien, C.-L., Dollimore, D., Doyle, B.L., Fultz, B., Goldman, A.I., Gronsky, R., et al., Eds.; John Wiley & Sons: New York, NY, USA, 2000; pp. 11d.1.1–11d.1.25.
7. Newbury, D.E.; Ritchie, N.W.M. Is Scanning Electron Microscopy/Energy Dispersive X-ray Spectrometry (SEM/EDS) Quantitative? *Scanning* **2013**, *35*, 141–168. [[CrossRef](#)] [[PubMed](#)]
8. Holwell, D.A.; Adeyemi, Z.; Ward, L.A.; Graham, S.D.; Smith, D.J.; McDonald, I.; Smith, J.W. Low temperature alteration and upgrading of magmatic Ni-Cu-PGE sulfides as a source for hydrothermal Ni and PGE ores: A quantitative approach using automated mineralogy. *Ore Geol. Rev.* **2017**, *91*, 718–740. [[CrossRef](#)]
9. Keulen, N.; Malkki, S.N.; Graham, S. Automated quantitative mineralogy applied to metamorphic rocks. *Minerals* **2019**. Submitted this volume.
10. Goldstein, J.I.; Newbury, D.E.; Michael, J.R.; Ritchie, N.W.M.; Scott, J.-H.J.; Joy, C.C. *Scanning Electron Microscopy and X-Ray Microanalysis*; Springer: New York, NY, USA, 2017; p. 550.
11. Keulen, N.; Schumacher, J.C.; Næraa, T.; Kokfelt, T.F.; Schersten, A.; Szilas, K.; van Hinsberg, V.J.; Schlatter, D.M.; Windley, B.F. Meso- and Neoarchaean geological history of the Bjørnesund and Ravns Storø Supracrustal Belts, southern West Greenland: Settings for gold enrichment and corundum formation. *Precambrian Res.* **2014**, *254*, 36–58. [[CrossRef](#)]
12. Windley, B.F.; Garde, A.A. Arc-generated blocks with crustal sections in the North Atlantic craton of West Greenland: New mechanisms of crustal growth in the Archaean with modern analogues. *Earth Sci. Rev.* **2009**, *93*, 1–30. [[CrossRef](#)]
13. Keulen, N.; Kokfelt, T.F. The Homogenisation Team, 2011. A Seamless, Digital, Internet-Based Geological Map of South-West and Southern West Greenland, 1:100 000, 61°30'–64°. Copenhagen: Geological Survey of Denmark and Greenland. Available online: <http://geuskort.geus.dk/gisfarm/svgrl.jsp> (accessed on 9 May 2018).
14. Keulen, N.; Stünitz, H.; Heilbronner, R. Healing microstructures of experimental and natural fault gouge. *J. Geophys. Res.* **2008**, *113*, B06205. [[CrossRef](#)]
15. Hombourger, C.; Outrequin, M. Quantitative Analysis and High-Resolution X-ray Mapping with a Field Emission Electron Microprobe. *Microsc. Today* **2013**, *21*, 10–15. [[CrossRef](#)]
16. McSwiggen, P. Characterisation of sub-micrometre features with the FE-EPMA. *IOP Conf. Ser. Mater. Sci. Eng.* **2014**, *55*, 012009. [[CrossRef](#)]
17. Fournelle, J.; Cathey, H.; Pinard, P.T.; Richter, S. Low voltage EPMA: Experiments on a new frontier in microanalysis—Analytical lateral resolution. *IOP Conf. Ser. Mater. Sci. Eng.* **2016**, *109*, 012003. [[CrossRef](#)]
18. Hovington, P.; Drouin, D.; Gauvin, R. CASINO: A new Monte Carlo Code in C Language for Electron Beam Interaction—Part 1: Description of the program. *Scanning* **1997**, *19*, 1–14. [[CrossRef](#)]

19. Drouin, D.; Couture, A.R.; Joly, D.; Tastet, X.; Aimez, V.; Gauvin, R. CASINO V2.42—A fast and Easy-to-use modeling tool for scanning electron microscopy and microanalysis users. *Scanning* **2007**, *29*, 92–101. [[CrossRef](#)]
20. Stünitz, H.; Fitzgerald, J.D. Deformation of granitoids at low metamorphic grade. II: Granular flow in albite-rich mylonites. *Tectonophysics* **1983**, *221*, 299–324.
21. Tullis, J.; Yund, R.A. Dynamic recrystallization of feldspar: A mechanism for ductile shear zone formation. *Geology* **1985**, *13*, 238–241. [[CrossRef](#)]
22. Velde, B.; Suzuki, T.; Nicot, E. Pressure-temperature of illite-smectite mixed-layer minerals: Niger delta mudstones and other examples. *Clays Clay Miner.* **1986**, *34*, 435–441. [[CrossRef](#)]
23. Kristmannsdottir, H. Alteration of Basaltic Rocks by Hydrothermal-Activity at 100–300 °C. *Dev. Sedim.* **1979**, *27*, 359–367.
24. Abd Emola, A.; Charpentier, D.; Bautier, M.; Lanari, P.; Monié, P. Textural-chemical changes and deformation conditions registered by phyllosilicates in a fault zone (Pic de Port Vieux thrust, Pyrenees). *Appl. Clay Sci.* **2017**, *144*, 88–103. [[CrossRef](#)]



© 2019 by the authors. Licensee MDPI, Basel, Switzerland. This article is an open access article distributed under the terms and conditions of the Creative Commons Attribution (CC BY) license (<http://creativecommons.org/licenses/by/4.0/>).